Article

aeroacoustics

Grid sensitivity of flow field and noise of high-Reynolds-number jets computed by large-eddy simulation

International Journal of Aeroacoustics
2018, Vol. 17(4–5) 399–424

DOI: 10.1177/1475472X18778287
journals.sagepub.com/home/jae
SAGE

Christophe Bogey

Abstract

Three isothermal round jets at a Mach number of 0.9 and a diameter-based Reynolds number of 10^5 are computed by large-eddy simulation using four different meshes in order to investigate the grid sensitivity of the jet flow field and noise. The jets correspond to two initially fully laminar jets and one initially strongly disturbed jet considered in previous numerical studies. At the exit of a pipe nozzle of radius r_0, they exhibit laminar boundary-layer mean-velocity profiles of thickness $0.2r_0$, $0.025r_0$ and $0.15r_0$, respectively. For the third jet, a peak turbulence intensity close to 9% is also imposed by forcing the boundary layer in the nozzle. The grids contain up to one billion points, and, compared to the grids used in previous simulations, they are finer in the axial direction downstream of the nozzle and in the radial direction on the jet axis and in the outer region of the mixing layers. The main flow field and noise characteristics given by the simulations, including the mixing-layer thickness, the centerline mean velocity, the turbulence intensities on the nozzle lip line and the jet axis, spectra of velocity and far-field pressure obtained from the jet near field by solving the isentropic linearized Euler equations, are presented. With respect to those from previous studies, the results are very similar for the initially laminar jet with thick boundary layers, but they differ significantly for the initially laminar jet with thin boundary layers and for the initially disturbed jet. For the latter two jets, using a finer grid leads to a faster flow development, to higher turbulence intensities in the shear layers and at the end of the potential core, to stronger large-scale structures, and to the generation of more low-frequency noise.

Univ Lyon, Ecole Centrale de Lyon, France

Corresponding author:
Christophe Bogey, Laboratoire de Mécanique des Fluides et d'Acoustique, UMR CNRS 5509, Ecole Centrale de Lyon, 69134 Ecully, France.
Email: christophe.bogey@ec-lyon.fr

Moreover, very small mesh spacings appear to be necessary all along the jet mixing layers, and in particular during their early stages of growth, to properly capture the formation and dynamics of the flow coherent structures and thus obtain results in good agreement with measurements available for high-Reynolds-number jets.

Keywords
Mixing layer, jet noise computation, large-eddy simulation, grid sensitivity, coherent structures

Date received: 29 November 2017; accepted: 25 February 2018

Introduction

Since the first developments in the field of computational aeroacoustics in the early nineties,[1] considerable progress has been made in the simulation of the flow and acoustic fields of high-speed turbulent jets,[2–5] which should help us to better describe the underlying noise generation mechanisms. For subsonic jets, in particular, a number of research teams[6–9] have been able to obtain far-field pressure spectra in good agreement with experimental measurements using different numerical methodologies. Nevertheless, for these flows, unlike other flows such as turbulent boundary layers, there is still no clear rule concerning the resolution required to obtain trustworthy solutions. This is due to the fact that even today simulating a jet is difficult and costly, because it has to deal with turbulent flow phenomena whose nature and scales strongly differ. These phenomena take place in the boundary layers in the jet nozzle, in the growing mixing layers, at the end of the potential core located around seven diameters downstream of the nozzle, and in the developed jet region farther downstream. They impose severe and sometimes contradictory constraints on the grid design. Furthermore, some flow phenomena, such as the merging of the mixing layers at the end of the potential core where intense sound sources are found,[10–13] are not very well understood, which makes their calculation uncertain.

In order to validate subsonic jet simulations, the usual approach consists in performing comparisons with experiments. However, these comparisons and their resulting interpretations must be taken with care. Indeed, the experimental data may be inaccurate due to measurement issues[14] and to acoustic reflections and contaminations.[15–17] For well-known or still-debated reasons, they may also vary significantly from one experiment to another.[18–20] Thus, it is fairly easy or, even worse, tempting to choose the sets of data that best match the numerical data to be validated. Among the reasons likely to cause differences between experiments, the effects of the Reynolds number $\mathrm{Re}_D = u_j D/\nu_j$, where $D = 2r_0$ is the jet nozzle diameter, and u_j and ν_j are the nozzle-exit velocity and kinematic molecular viscosity, respectively, and of the initial flow conditions can be emphasized. It has for instance been shown that a Reynolds number $\mathrm{Re}_D \geq 4 \times 10^5$ is required to avoid the effects associated with low Reynolds number.[19] Therefore, the simulations of jets at a low Reynolds number[21–23] should only be compared with experiments at the same Reynolds number, and the simulations of jets at a high Reynolds number may provide irrelevant results if exceedingly dissipative numerical methods are employed. Concerning the influence of the initial

conditions, it has been established that more noise is generated in initially laminar jets than in initially turbulent jets, due to the pairings of large coherent structures in the mixing layers of the former jets.[24–28] Consequently, the jet initial conditions in the simulations and the experiments should be identical to carry out meaningful comparisons. Unfortunately, it is rarely feasible due to the limited experimental databases and computational resources available.

Another approach recommended for the validation of simulation accuracy consists in comparing solutions obtained over a range of different grid resolutions in order to demonstrate that the results are grid-independent or grid-convergent. Such studies should be mandatory, but in practice they are very difficult to do because of their prohibitive cost for fully three-dimensional turbulent flows. In these studies, in addition, there is a need to ensure that the solutions are converged in time, and that the initial conditions do not change when the grid is refined, which may not be simple. For subsonic jets at a Mach number of $M = u_j/c_a = 0.9$, where c_a is the speed of sound in the ambient medium, few grid convergence studies have been conducted. Exceptions include the work by Shur et al.,[6,29] Bogey and Bailly,[27] Bogey et al.,[30] Bühler et al.,[23] and Brès et al.[9] In Shur et al.,[6] four grids containing up to 23 million points were considered for a jet at $Re_D = 1.1 \times 10^6$. Grid independence was not reached, and the finest grid leads to some overestimation of the length of the potential core compared to experiments. In Bogey et al.,[30] five grids were used to simulate a jet at $Re_D = 10^5$ with tripped nozzle-exit boundary layers. The grid resolutions differed mainly in the boundary layers inside the nozzle and in the shear layers just downstream. Hence, the solutions obtained using the fifth grid of 251 million points were shown to be nearly converged with respect to the grid in the shear layers up to $z = 4r_0$ in the downstream direction, but no solid evidence of their accuracy further downstream was given. This is a pity because in subsonic jets, according to experiments,[31–37] high-frequency sound sources are located near the nozzle exit, whereas low-frequency sources lie farther downstream. In cold jets,[36] for instance, peak source locations are noted around $z = 6r_0$ for Strouhal number $St_D = fD/u_j = 2$, where f is the frequency, but around $z = 12r_0$ for $St_D = 0.5$, and $z = 22r_0$ for $St_D = 0.15$, that is approximately the peak Strouhal number in the spectra measured in the jet direction.[37–39] As a result, the grid resolution in simulations must remain fine enough over a very large spatial extent in the axial direction.

In the present work, three isothermal round jets at a Mach number of $M = 0.9$ and a Reynolds number of $Re_D = 10^5$ are computed by large-eddy simulation (LES) using several grids in order to investigate the grid dependence of the jet flow field and noise. The jets originate at $z = 0$ from a straight pipe nozzle. They correspond to three jets examined in earlier studies,[27,30] namely two initially fully laminar jets with thick and thin nozzle-exit boundary layers, respectively, and an initially strongly disturbed jet in which a forcing is applied to the boundary layers inside the nozzle to generate a high level of turbulent fluctuations at the exit. Four cylindrical grids, containing from 250 million to one billion points, are used. Their resolutions are identical in the upstream boundary layers and in the shear layers very near to the nozzle exit, but different in the other flow regions, notably in the developing mixing layers, and around and downstream of the end of the jet potential core. The results obtained for the four grids are compared between each others, with the results from previous studies using coarser grids, and with experimental data of the literature for high-Reynolds-number jets. The objectives of this work are therefore to determine whether the characteristics of the flow and acoustic fields calculated on the present grids are similar or not, to display and quantify their differences with respect to the previous results,

and to identify the grid point distribution providing the results in best agreement with measurements, in particular for the initially strongly disturbed jet.

The paper is organized as follows. The main characteristics of the different jets and of the simulations, including inflow conditions, numerical methods, grid and computational parameters, are first documented. Vorticity snapshots, nozzle-exit flow velocity profiles, mean and fluctuating velocity profiles obtained along the nozzle lip line and the jet centerline are then presented. Pressure snapshots and spectra calculated in the acoustic far field are reported. Finally, concluding remarks are given.

Parameters

Jet definition

Three isothermal round jets, referred to as jetv0D0200, jetv0D0025 and jetv9D0150, are simulated. They correspond to jets considered in previously in Bogey and Bailly[27] in the first two cases, and in Bogey et al.[30] in the latter case. They have a Mach number of $M = 0.9$ and a Reynolds number of $Re_D = 10^5$, as reported in Table 1. The ambient temperature and pressure are $T_a = 293$ K and $p_a = 10^5$ Pa, respectively. The jets originate from a pipe nozzle of radius r_0 and length $2r_0$. The pipe exit is at $z = 0$, and the pipe wall thickness is $0.053r_0$. At the pipe inlet, at $z = -2r_0$, a Blasius laminar boundary-layer profile of thickness δ_{BL} is imposed for the axial velocity.[27] Radial and azimuthal velocities are set to zero, pressure is equal to p_a, and temperature is determined by a Crocco-Busemann relation.

The three jets are chosen in order to study the grid sensitivity of the LES results over a wide range of jet initial conditions. In particular, the nozzle-exit parameters of the first jet are very unlikely to be encountered in experiments for jets at Reynolds numbers equal to or higher than 10^5. It is however considered in order to demonstrate that the grid sensitivity depends on the inflow conditions imposed in the jet simulations. The boundary-layer thickness δ_{BL} at the pipe nozzle inlet and the peak turbulence intensity u'_e/u_j reached at the exit in the different cases are given in Table 1. The first two jets are both initially fully laminar with u'_e/u_j close to 0%, but the boundary layers are thick in jetv0D0200 and thin in jetv0D0025, with $\delta_{BL} = 0.2r_0$ and $\delta_{BL} = 0.025r_0$, respectively. The boundary layers of jetv9D0150 are also rather thick with $\delta_{BL} = 0.15r_0$, but they are tripped in order to generate highly disturbed exit conditions, which would otherwise be laminar, as is usually done in laboratory experiments.[24–26,40] In practice, random low-level vortical disturbances uncorrelated in the azimuthal direction are added at $z = -0.95r_0$ inside the pipe, following the procedure detailed in Bogey et al.[30] The forcing strength used in the present simulations is that empirically set in the previous LES[30] of jetv9D0150 to obtain a peak turbulence intensity of 9% at

Table 1. Jet parameters: Mach and Reynolds numbers M and Re_D, thickness of the Blasius laminar boundary-layer profile imposed at the pipe nozzle inlet δ_{BL}, peak turbulence intensity at the nozzle exit u'_e/u_j.

Jet	M	Re_D	δ_{BL}	u'_e/u_j
jetv0D0200	0.9	10^5	$0.200r_0$	0%
jetv0D0025	0.9	10^5	$0.025r_0$	0%
jetv9D0150	0.9	10^5	$0.150r_0$	9%

the nozzle exit, while keeping a mean velocity profile close to the inlet laminar boundary-layer profile. Finally, random pressure fluctuations are introduced in the jet shear layers initially at time $t = 0$ in order to reduce the initial transitory period.

In what follows, the simulation results will be compared with measurements available for jets at Reynolds numbers $\mathrm{Re}_D \simeq 10^6$. At such high Reynolds numbers, the initial state of the jets should not be laminar, but highly disturbed or turbulent. Therefore, a good agreement between LES and experimental data is only expected for jetv9D0150.

LES approach and numerical methods

The numerical framework is identical to that used in recent jet simulations,[27,28,30,41–43] including the previous simulations of jetv0D0200, jetv0D0025 and jetv9D0150. The LES are carried out using an in-house solver of the three-dimensional filtered compressible Navier–Stokes equations in cylindrical coordinates (r, θ, z) based on low-dissipation and low-dispersion explicit schemes. The axis singularity is taken into account by the method of Mohseni and Colonius.[44] In order to alleviate the time-step restriction near the cylindrical origin, the derivatives in the azimuthal direction around the axis are calculated at coarser resolutions than permitted by the grid.[45] For the points closest to the jet axis, they are evaluated using n_θ^{axis} points, yielding an effective resolution of $2\pi/n_\theta^{axis}$. Fourth-order eleven-point centered finite differences are used for spatial discretization, and a second-order six-stage Runge–Kutta algorithm is implemented for time integration.[46] A sixth-order eleven-point centered filter[47] is applied explicitly to the flow variables every time step. Non-centered finite differences and filters are also used near the pipe walls and the grid boundaries.[48,27] At the boundaries, the radiation conditions of Tam and Dong[49] are applied, with the addition at the outflow of a sponge zone combining grid stretching and Laplacian filtering,[50] to avoid significant acoustic reflections. Small adjustment terms are also added to prevent that mean density and pressure deviate significantly from ambient density and pressure, but no co-flow is imposed.

In the present LES, the explicit filtering is employed to remove grid-to-grid oscillations, but also as a subgrid-scale high-order dissipation model in order to relax turbulent energy from scales at wave numbers close to the grid cut-off wave number while leaving larger scales mostly unaffected. The performance of this LES approach has been assessed in past studies for subsonic jets, Taylor–Green vortices and turbulent channel flows,[30,51–54] from comparisons with solutions of direct numerical simulations and from the examination of the magnitude and the properties of the filtering dissipation in the wavenumber space.

Grid parameters

Four cylindrical grids, referred to as gridz60A, gridz40A, gridz40B and gridz25B, are designed in this work. Due to the high numerical cost, they are not refined in a systematic manner. In this way, this work is not a grid convergence study, whose results, however, would depend on the first mesh arbitrarily built. The main characteristics of the grids are collected in Table 2. Those of the grids used in previous simulations[27,30] for jetv0D0200, jetv0D0025 and jetv9D0150, and in a recent study[8] for two jets at $\mathrm{Re}_D = 2 \times 10^5$, denoted as gridv0D0200old, gridv0D0025old, gridv9D0150old and grid3Mpts, are also given for comparison. The present grids have similar numbers of points in the radial and axial directions, namely $n_r \simeq 500$ and $n_z \simeq 2000$, and sizes decreasing with the resolution. Thus, the physical

Table 2. Parameters of the present grids (gridz60A, gridz40A, gridz40B and gridz25B) and of grids used in previous studies (gridv0D0200old[27], gridv0D0025old[27], gridv9D0150old[30,28, 42] and grid3Mpts[8]): numbers of points n_r and n_z and extents of the physical domain L_r and L_z in the radial and axial directions, effective number of points n_θ^{axis} in the azimuthal direction close to the jet axis, and mesh spacings Δr and Δz at different positions.

				$\Delta r/r_0$ (%) at $r =$				$\Delta z/r_0$ (%) at $z =$				
Grid	n_r, n_z	L_r, L_z	n_θ^{axis}	0	r_0	$2r_0$	$4r_0$	0	$5r_0$	$10r_0$	$15r_0$	$25r_0$
gridz60A	512, 1908	$20r_0$, $60r_0$	32	2.92	0.36	2.93	3.86	0.72	2.83	3.11	3.39	3.96
gridz40A	495, 1977	$15r_0$, $40r_0$	16	1.89	0.36	2.37	3.31	0.72	2.39	2.39	2.39	2.39
gridz40B	504, 2085	$15r_0$, $40r_0$	16	1.41	0.36	1.48	3.35	0.72	1.27	1.78	2.30	3.33
gridz25B	504, 2085	$9r_0$, $25r_0$	16	1.14	0.36	1.25	2.54	0.72	1.07	1.38	1.69	2.31
gridv0D0200old	173, 502	$8.2r_0$, $20r_0$	8	2.90	2.90	5.25	5.51	5.80	5.80	5.80	5.80	5.80
gridv0D0025old	287, 651	$8.6r_0$, $25r_0$	8	2.92	0.36	3.74	5.65	0.72	5.77	5.77	5.77	5.77
gridv9D0150old	249, 962	$6.75r_0$, $25r_0$	16	2.92	0.36	3.74	8.15	0.72	2.83	5.09	6.56	6.56
grid3Mpts	496, 3052	$8.4r_0$, $28.4r_0$	32	1.54	0.15	1.83	5	0.31	0.74	1.18	1.62	2.50

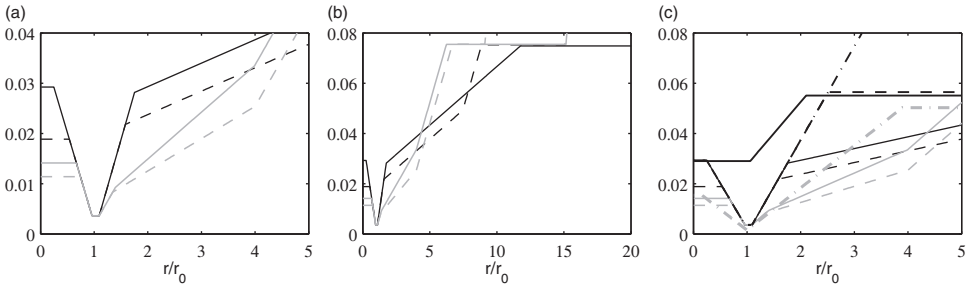

Figure 1. Variations of the radial mesh spacing $\Delta r/r_0$ (a) over $0 \leq r \leq 5r_0$ and (b) over $0 \leq r \leq 20r_0$ for ——— gridz60A, – – – gridz40A, ——— gridz40B, – – – gridz25B, and (c) over $0 \leq r \leq 5r_0$ for the present grids and ——— gridv0D0200old, – – – gridv0D0025old – · – · gridv9D0150old and – · – · grid3Mpts.

extents of gridz60A, gridz40A, gridz40B and gridz25B are respectively equal to $L_z = 60r_0$, $40r_0$, $40r_0$ and $25r_0$ in the axial direction, and to $L_r = 20r_0$, $15r_0$, $15r_0$ and $9r_0$ in the radial direction. According to experimental results,[31–37] the jet noise sources are expected to be fully captured on the first three grids, but it might not be the case for low-frequency sources typically below $\mathrm{St}_D = 0.2$ on gridz25B, due to the limited extent in the axial direction in this case. For all grids, the number of points n_θ in the azimuthal direction can be set to 256, 512 or 1024. Moreover, for stability concerns, the effective number of points n_θ^{axis} close to the jet axis must be reduced to 32 for gridz60A, and 16 for gridz40A, gridz40B and gridz25B.

The variations of the radial and axial mesh spacings Δr and Δz in the different grids are represented in Figures 1 and 2. In order to specify the same initial flow conditions in the previous and present simulations of jetv9D0150 with tripped nozzle-exit boundary layers, the four grids are derived from gridv9D0150old. More precisely, they are identical to gridv9D0150old for $0.75r_0 \leq r \leq 1.1r_0$ and $z \leq 0.4r_0$, with mesh spacings $\Delta r = 0.0036r_0$ at $r = r_0$ and $\Delta z = 0.0072r_0$ at $z = 0$ in all cases. Elsewhere, they are similar to or

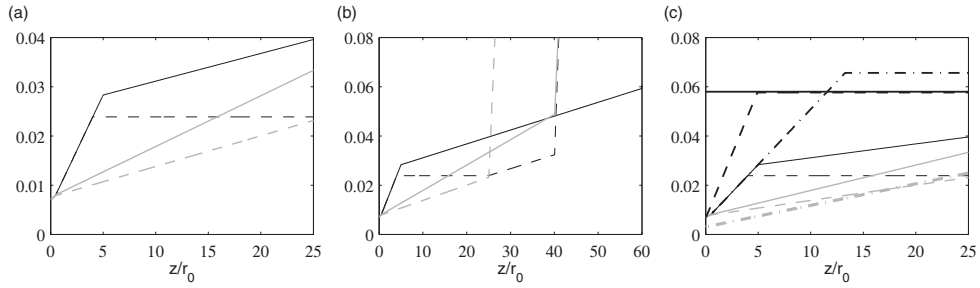

Figure 2. Variations of the axial mesh spacing $\Delta z/r_0$ (a) over $0 \leq z \leq 25r_0$ and (b) over $0 \leq z \leq 60r_0$ for ——— gridz60A, — — — gridz40A, ——— gridz40B, — — — gridz25B, and (c) over $0 \leq z \leq 25r_0$ for the present grids and ——— gridv0D0200old, — — — gridv0D0025old — · — · gridv9D0150old and — · — · grid3Mpts.

more refined than gridv9D0150old. In the radial direction, the mesh spacings Δr at $r = 0$ and $r = 2r_0$ range from $0.0292r_0$ and $0.0293r_0$ in gridz60A down to $0.0114r_0$ and $0.0125r_0$ in gridz25B, whereas they are equal to $0.0292r_0$ and $0.0374r_0$ in gridv9D0150old. The difference in resolution is also very significant at $r = 4r_0$, where Δr is found to be $0.0335r_0$ in gridz40B and $0.0815r_0$ in gridv9D0150old, for instance. In the axial direction, the mesh spacings Δz at $z = 10r_0$ and $z = 25r_0$ vary from $0.0311r_0$ and $0.0396r_0$ in gridz60A down to $0.0138r_0$ and $0.0231r_0$ in gridz25B, with $\Delta z = 0.0509r_0$ and $0.0656r_0$ in gridv9D0150old. Compared to the previous grids, as also shown in Figures 1(c) and 2(c), the present grids are much finer in the radial direction on the jet axis and in the outer region of the mixing layers, and in the axial direction, notably between $z = 10r_0$ and $z = 25r_0$ where the most significant noise sources of cold jets at $M = 0.9$ are located according to experimental results.[36] In the axial direction, the resolution increase with respect to gridv9D0150old however starts at $z = 5r_0$ and $4r_0$ for gridz60A and gridz40A, but at $z = 0.5r_0$ and $0.4r_0$ for gridz40B and gridz25B, leading to $\Delta z = 0.0283r_0$ for gridz60A and $0.0127r_0$ for gridz40B at $z = 5r_0$, for example. Therefore, the mixing layers developing early on in the jets are better discretized using the last two grids than the first two ones. Finally, the maximal mesh spacing in the physical part of the computational domains, for $r \leq L_r$ and $z \leq L_z$, is equal to $\Delta r = 0.075r_0$, yielding a Strouhal number of $St_D = 5.9$ for an acoustic wave with five points per wavelength.

Simulation parameters

As reported in Table 3, each of the three jets in this work is computed using gridz60A, gridz40A, gridz40B and gridz25B. The time step is the same in the twelve cases considered. In order to ensure numerical stability, it is based on the minimum mesh spacing, and is defined by $\Delta t = 0.7 \times \Delta r(r = r_0)/c_a$, yielding $\Delta t = 0.0011 \times D/u_j$, which is very small. Therefore, given the very low dissipation and dispersion of the Runge–Kutta scheme used, significant time-integration errors are highly unlikely in the present simulations.

The grids contain $n_r \times n_\theta \times n_z \simeq 250$ million points for jetv0D0200, 500 million points for jetv0D0025, and one billion points for jetv9D0150, using $n_\theta = 256$, 512 and 1024 points in the azimuthal direction, respectively, depending on the jet initial conditions.[30] As a result, the simulations of the two initially fully laminar jets are faster and could run over a longer

Table 3. Simulation parameters: grids used, number of points in the azimuthal direction n_θ, total number of points, and simulation time T after the transient period.

Jet	Grid	n_θ	$n_r \times n_\theta \times n_z$	Tu_j/r_0
jetv0D0200	gridz60A	256	2.5×10^8	900
jetv0D0200	gridz40A	256	2.5×10^8	600
jetv0D0200	gridz40B	256	2.7×10^8	600
jetv0D0200	gridz25B	256	2.7×10^8	600
jetv0D0025	gridz60A	512	5×10^8	600
jetv0D0025	gridz40A	512	5×10^8	600
jetv0D0025	gridz40B	512	5.4×10^8	450
jetv0D0025	gridz25B	512	5.4×10^8	450
jetv9D0150	gridz60A	1024	10^9	300
jetv9D0150	gridz40A	1024	10^9	300
jetv9D0150	gridz40B	1024	1.1×10^9	300
jetv9D0150	gridz25B	1024	1.1×10^9	300

period than those of the tripped jet, providing results better converged in time. For the grids of one billion points, 200 GB of memory are required, and about 1000 CPU hours are needed for 1000 iterations using an OpenMP-based in-house solver. Since between 300,000 and 700,000 iterations are performed in each case, a total number of about 3 billion CPU hours is consumed.

The simulation time T after the transient period is equal to $900r_0/u_j$ using gridz60A and $600r_0/u_j$ using the three other grids for jetv0D0200, to $600r_0/u_j$ using gridz60A and gridz40A and $450r_0/u_j$ otherwise for jetv0D0025, and to $300r_0/u_j$ for jetv9D0150 in all cases. During that time, density, velocity components and pressure along the jet axis at $r = 0$, and on the surfaces located at $r = r_0$, $r = 15r_0$ (except for gridz25B) and $r = L_r$ and at $z = -1.5r_0$, $z = 0$, $z = 15r_0$, $z = 30r_0$ (except for gridz25B) and $z = L_z$, are recorded at a sampling frequency allowing spectra to be computed up to $\mathrm{St}_D = 12$. Density, velocities and pressure obtained at the azimuthal angles $\theta = 0$, 90, 180 and 270 degrees are also stored at a halved frequency. The flow and acoustic near field statistics presented in the next sections are calculated from these recordings. They are averaged in the azimuthal direction, when possible. Time spectra are evaluated from overlapping samples of duration $45r_0/u_j$ on the jet axis, and $90r_0/u_j$ otherwise. In the azimuthal direction, post-processing can be performed up to the mode $n_\theta = 128$, where n_θ is the dimensionless azimuthal wave number such that $n_\theta = k_\theta r$.

Far-field extrapolation

The LES near-field fluctuations are propagated to the acoustic far field using an in-house OpenMP-based solver of the isentropic linearized Euler equations (ILEEs) in cylindrical coordinates,[55] as illustrated in Figure 3. By replacing the ILEE with the weakly non-linear or the full Euler equations, this solver also offers the opportunity to investigate non-linear propagation effects, as was done in a previous study for a highly supersonic jet.[56]

The extrapolation is performed from the velocity and pressure fluctuations obtained at $z = -1.5r_0$, $r = L_r$ and $z = L_z$ in the jet simulations, recorded over the time periods given in

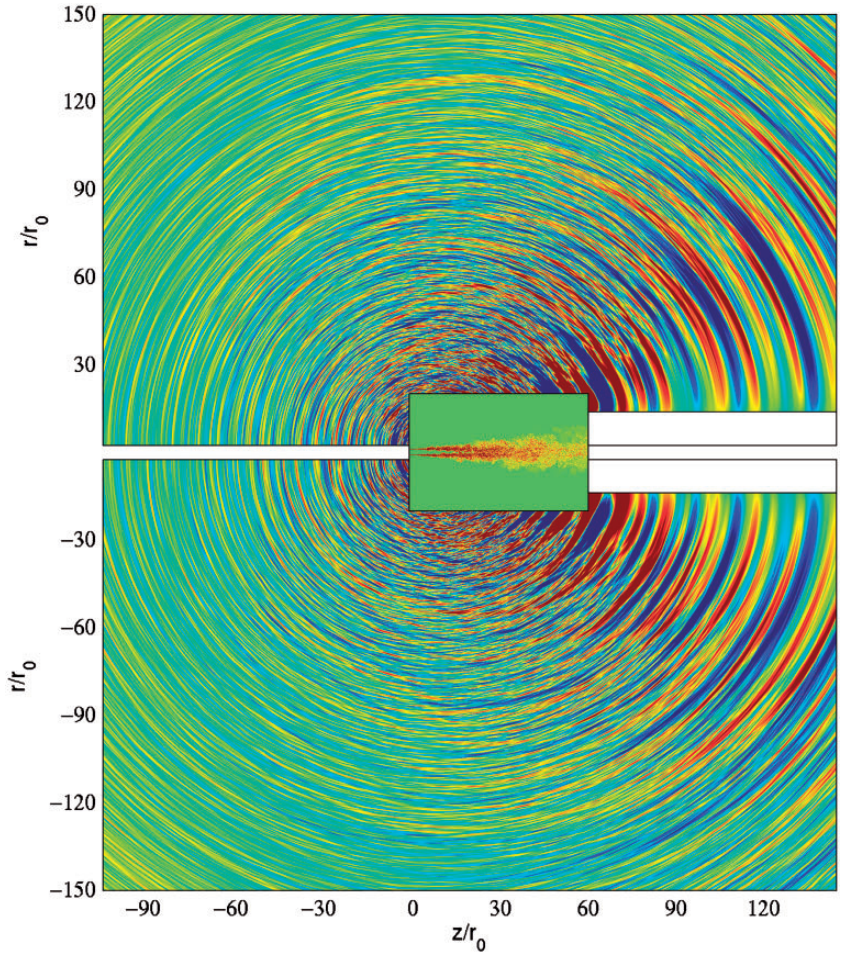

Figure 3. Representation of vorticity norm obtained inside the LES domain for jetv9D0150 using gridz60A and of pressure fluctuations extrapolated outside by solving the ILEE. The color scales range up to the level of $4u_j/r_0$ for vorticity, and from –7 to 7 Pa for pressure (See colour version of this figure online).

Table 3 at a sampling frequency corresponding to $\mathrm{St}_D = 12$. The same numerical methods as in the LES, and a grid containing $n_r \times n_\theta \times n_z = 2048 \times 256 \times 3506 = 1.8$ billion points are used. Excluding the eighty-point sponge zones implemented at the upstream, downstream and outer radial boundaries to minimize acoustic reflections, the grid extends axially from $z = -106r_0$ up to $z = 145r_0$ and radially from $r = 2.5r_0$ up to $r = 151r_0$. In this region, the radial and axial mesh spacings are constant and equal to $\Delta r = \Delta z = 0.075r_0$, yielding $\mathrm{St}_D = 5.9$ for an acoustic wave discretized by five points per wavelength. The near-field fluctuations are interpolated and imposed onto the grid at $z = -1.5r_0$ between $r = 2.5r_0$ and $r = L_r$, at $r = L_r$ between $z = -1.5r_0$ and $z = L_z$, and at $z = L_z$ between $r = r_{min}$ and $r = L_r$, where $r_{min} = 13.85r_0$, $9.23r_0$, $9.23r_0$ and $6.68r_0$ for the LES using gridz60A, gridz40A, gridz40B and gridz25B, respectively. The extrapolation surface is open in the downstream direction, in order to avoid the presence of aerodynamic disturbances,[57] which may cause

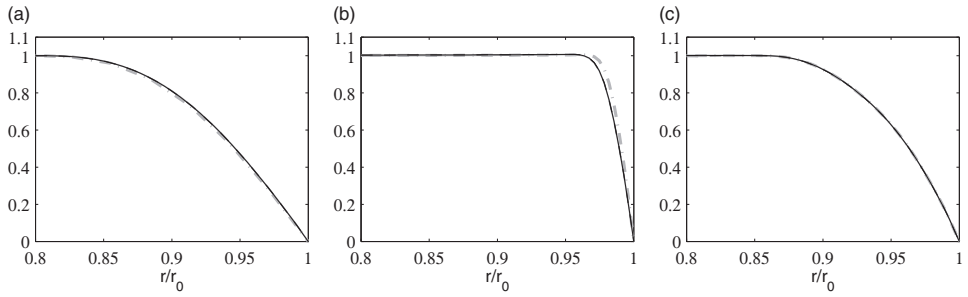

Figure 4. Nozzle-exit radial profiles of mean axial velocity $\langle u_z \rangle / u_j$ obtained for (a) jetv0D0200, (b) jetv0D0025, and (c) jetv9D0150 using ——— gridz60A, — — — gridz40A, ——— gridz40B, — — — gridz25B, — · — · coarser grids (gridv0D0200old for jetv0D0200, gridv0D0025old for jetv0D0025 and gridv9D0150old for jetv9D0150) in previous studies.

low-frequency spurious waves as in previous studies.[8,27,30] However, the opening angle relative to the jet direction, with the nozzle exit as an origin, is only $\varphi = 13$ degrees in the first three cases and 15 degree in the fourth one, which should allow most of the downstream noise components to be taken into account. Each ILEE computation requires 200 GB of memory, and lasts during between 5000 and 12,000 iterations, resulting to a total number of about 100,000 CPU hours consumed. Pressure is recorded at a distance of $150r_0$ from $z = r = 0$ where far-field acoustic conditions are expected to apply according to measurements,[58,59] as in the experiment of Bridges and Brown,[16] for angles between $\varphi = 15$ degrees and $\varphi = 135$ degrees. Pressure spectra are evaluated using overlapping samples of duration $90r_0/u_j$, and they are averaged in the azimuthal direction.

Jet flow fields

Nozzle-exit velocity profiles

The mean and rms axial velocity profiles obtained at the nozzle-exit section of the three jets in the present simulations are presented in Figures 4 and 5.

The profiles calculated using gridz60A, gridz40A, gridz40B and gridz25B are superimposed, indicating that the initial conditions of the jets do not change with the grid. This is particularly true in Figures 4(c) and 5(c) for jetv9D0150, whose upstream boundary layers are forced inside the nozzle to generate significant exit velocity fluctuations. Furthermore, the results agree with those from previous LES performed using coarser grids, also shown in the figures. A small difference can however be noted in Figure 4(b) for the mean velocity profile of jetv0D0025, which is slightly thinner in the simulation using gridv0D0025old.

The nozzle-exit mean velocity profiles are similar to the laminar profiles imposed at the nozzle inlet, and has momentum thicknesses of $\delta_\theta = 0.0237r_0$ in jetv0D0200, $\delta_\theta = 0.0036r_0$ in jetv0D0025 and $\delta_\theta = 0.0185r_0$ in jetv9D0150. Compared to experiments,[60] the jet boundary layers are thick in the first and third case, and thin in the second case. The peak turbulence intensities u'_e/u_j are close to 0.2% in jetv0D0200 and to 0.3% in jetv0D0025, and they are equal to 9.1% in jetv9D0150. The first two jets are thus initially fully laminar, whereas the third one is initially highly disturbed, but not fully turbulent. The nozzle-exit conditions in the latter jet are comparable to those measured by Zaman[24,25] in a tripped jet

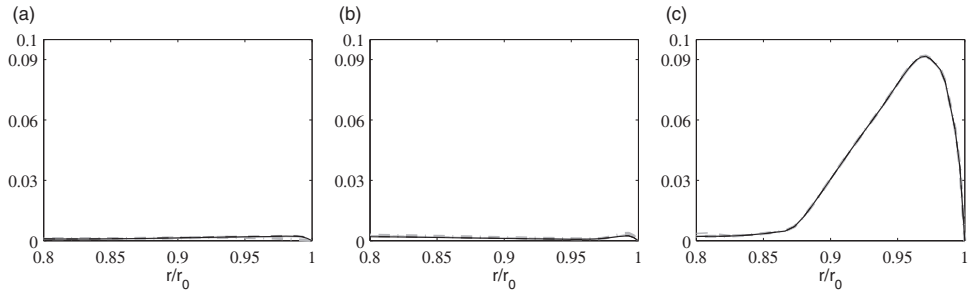

Figure 5. Nozzle-exit radial profiles of axial turbulence intensity $\langle u_z' u_z' \rangle^{1/2}/u_j$ obtained for (a) jetv0D0200, (b) jetv0D0025 and (c) jetv9D0150; same line types as in Figure 4.

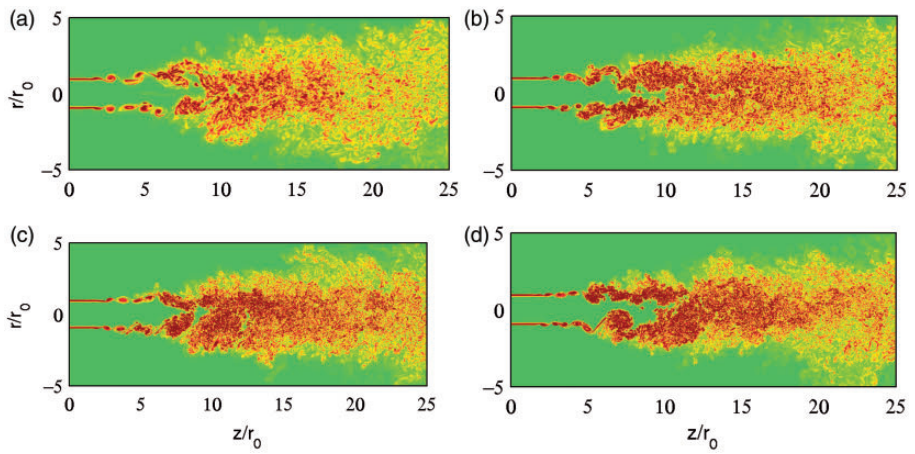

Figure 6. Representation of vorticity norm obtained for jetv0D0200 using (a) gridv9D0150old, (b) gridz60A, (c) gridz40A and (d) gridz40B. The color scale ranges up to the level of $6.5u_j/r_0$ (See colour version of this figure online).

at $\mathrm{Re}_D = 10^5$. They are discussed in more detail in a paper[41] providing velocity spectra as a function of axial and azimuthal wavenumbers.

Vorticity snapshots

Snapshots of the vorticity norm calculated between $z = 0$ and $z = 25r_0$ for the three jets using gridz60A, gridz40A and gridz40B are represented in Figures 6(b–d), 7(b–d) and 8(b–d). For the comparison, vorticity snapshots from the previous studies using coarser grids are displayed in Figures 6(a), 7(a) and 8(a). In the two jets with fully laminar upstream conditions, as expected,[27,28] roll-ups and pairings of vortical structures are observed downstream of the nozzle. The initially laminar jet with thick nozzle-exit boundary layers also develops more rapidly than the two others, leading to a potential core ending around $z = 10r_0$ in jetv0D0200, but around $z = 15r_0$ in jetv0D0025 and jetv9D0150.

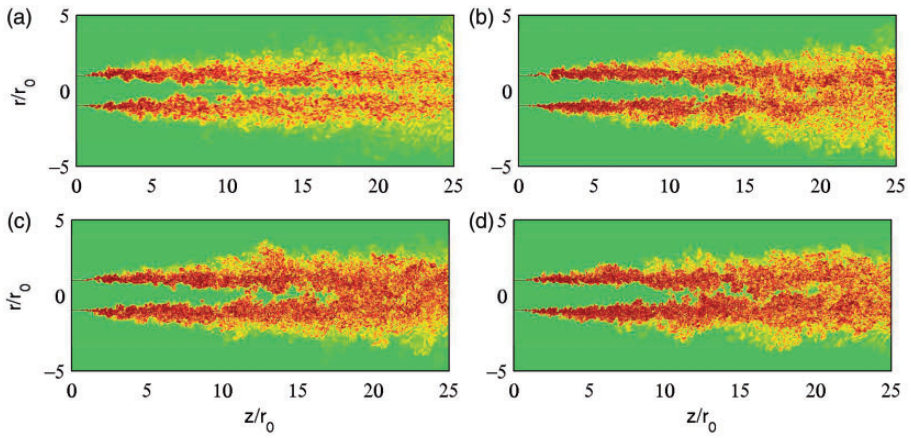

Figure 7. Representation of vorticity norm obtained for jetv0D0025 using (a) gridv0D00250ld, (b) gridz60A, (c) gridz40A and (d) gridz40B. The color scale ranges up to the level of $6.5u_j/r_0$ (See colour version of this figure online).

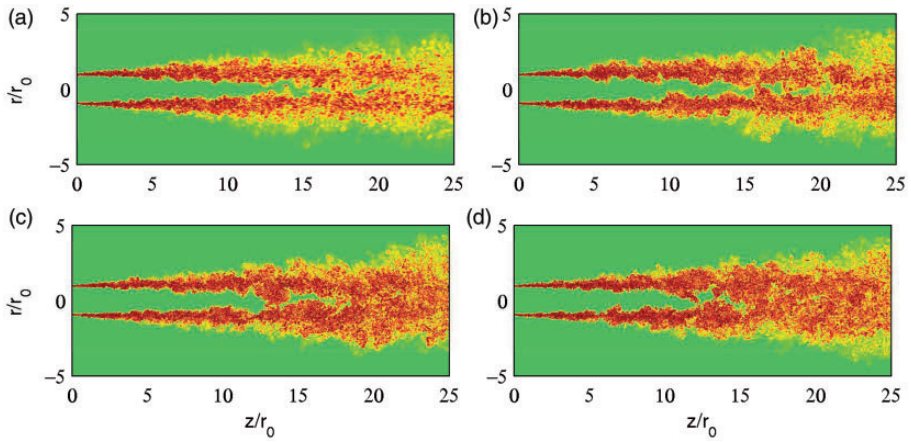

Figure 8. Representation of vorticity norm obtained for jetv9D0150 using (a) gridv9D0150old, (b) gridz60A, (c) gridz40A and (d) gridz40B. The color scale ranges up to the level of $6.5u_j/r_0$ (See colour version of this figure online).

While these snapshots must be interpreted with caution, they suggest that the effects of the grid on the vorticity field are rather small for jetv0D0200, but significant for the two other jets, see for instance Figures 7(a,d) and 8(a,d) obtained for jetv0D0025 and jetv9D0150 using the grids of previous studies and gridz40B. When a finer grid is used, the vorticity levels are found to increase spectacularly, especially near the jet centerline and in the outer lateral flow regions. In addition, two flow features of importance in terms of jet development and noise generation are more clearly visible. The first one is the merging of the shear layers on the jet axis downstream of the jet core, which is for instance very difficult to see in Figure 7(a) for jetv0D0025 and in Figure 8(a) for jetv9D0150. The second one concerns the formation of large-scale structures in the turbulent mixing layers upstream of the

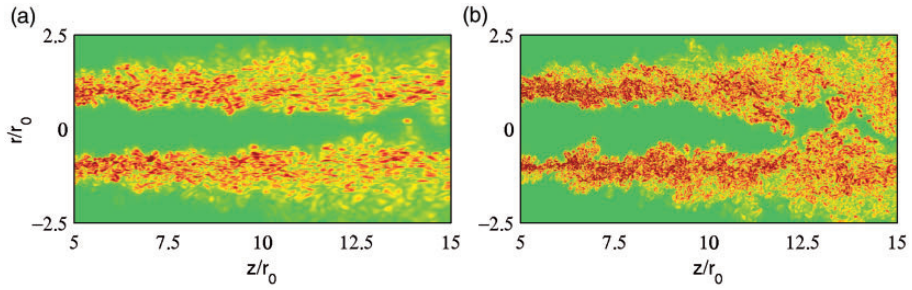

Figure 9. Representation of vorticity norm obtained for jetv9D0150 using (a) gridv9D0150old and (b) gridz40B. The color scale ranges up to the level of $14u_j/r_0$ (See colour version of this figure online).

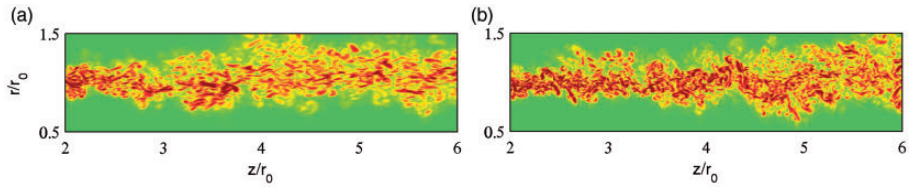

Figure 10. Representation of vorticity norm obtained for jetv9D0150 using (a) gridz40A and (b) gridz40B. The color scale ranges up to the level of $24u_j/r_0$ (See colour version of this figure online).

end of the potential core, resembling the coherent structures revealed by the visualizations of Brown and Roshko.[61]

The strong influence of the grid on these structures is further illustrated by Figure 9(a,b) showing the vorticity fields obtained between $z = 5r_0$ and $z = 15r_0$ for jetv9D0150 using gridv9D0150old and gridz40B. The presence of large-scale structures is more obvious in the latter case than in the former. A similar observation can be made for the vorticity fields of Figure 10(a,b) calculated between $z = 2r_0$ and $z = 6r_0$ for the same jet as previously using gridz40A and gridz40B. The use of smaller mesh spacings downstream of the nozzle in gridz40B, and consequently the computation of finer turbulent scales in that flow region, appear to allow the coherent structures in the mixing layer to be better captured.

Shear-layer properties

The variations over $0 \leq z \leq 20r_0$ of the shear-layer momentum thickness δ_θ in the three jets are presented in Figure 11. As examples, the experimental data obtained by Fleury[62] and Castelain[63] in isothermal jets at $M = 0.9$ and $Re_D \geq 7.7 \times 10^5$ are also shown. The shear layers develop very rapidly in the initially laminar jet with thick exit boundary layers, but at a lower rate in the two other jets with thin boundary layers, which is comparable to that in the experiments. Above all, for the three jets, the different curves obtained using the present and previous grids are very similar. However, for the initially disturbed jet, the mixing layer spreads slightly faster using gridz40B and gridz25B than the other grids in Figure 11(c), resulting in a better agreement with the measurements.

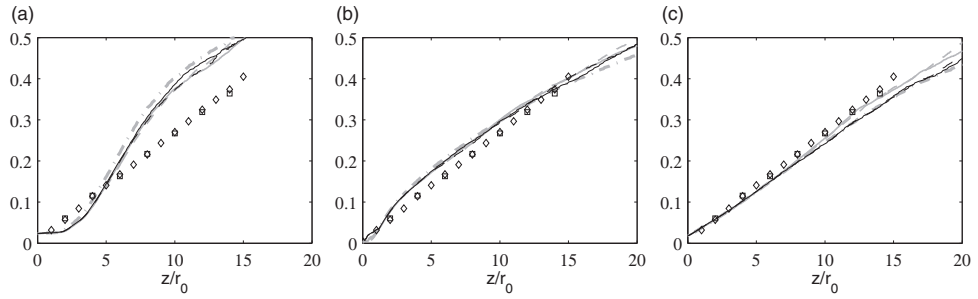

Figure 11. Variations of shear-layer momentum thickness δ_θ/r_0 obtained for (a) jetv0D0200, (b) jetv0D0025 and (c) jetv9D0150 using ——— gridz60A, — — — gridz40A ——— gridz40B, — — — gridz25B, — · — · coarser grids (gridv0D0200old for jetv0D0200, gridv0D0025old for jetv0D0025 and gridv9D0150old for jetv9D0150) in previous studies; measurements for isothermal jets at M = 0.9 of ◇ Fleury[62] at $Re_D = 7.7 \times 10^5$, and □ Castelain[63] at $Re_D = 10^6$.

The rms values of axial and radial velocity fluctuations estimated along the nozzle-lip line at $r = r_0$ between $z = 0$ and $z = 20r_0$ are displayed in Figures 12 and 13, respectively. As in the preceding figure, measurements for isothermal, Mach 0.9 jets at high Reynolds numbers are also drawn. Note that they represent peak rms values and not rms values at $r = r_0$. The influence of the initial jet flow state on the axial evolution of the turbulence intensities is clearly visible.[28] Indeed, a well-marked peak appears downstream of the nozzle exit in jetv0D0200 and jetv0D0025, whereas a monotonic growth, followed by a region of nearly constant values, is observed in jetv9D0150. The peak in the two initially laminar jets is due to the first stage of pairing of shear-layer Kelvin–Helmholtz vortices.

Concerning the sensitivity to the grid, the rms velocity profiles obtained for jetv0D0200 using gridz60A, gridz40A, gridz40B and gridz25B are practically all superimposed, and do not significantly differ from those from the simulation performed on gridv0D0200old. Those for jetv0D0025 and jetv9D0150 exhibit more remarkable discrepancies. First, compared to the previous studies using coarser grids, the turbulence intensities at large distances from the nozzle exit are stronger in the present LES. For instance, values of $\langle u_z' u_z' \rangle\rangle^{1/2}/u_j = 15.6\%$ and 12.9% are found at $z = 15r_0$ for jetv0D0025 using gridz40A and gridv0D0025old, respectively. Second, the fluctuation levels calculated using the two grids refined over $0 \leq z \leq 10r_0$, gridz40B and gridz25B, are slightly higher than those obtained using gridz60A and gridz40A. This is particularly true in the initially turbulent jet between $z = 5r_0$ and $z = 15r_0$. In this flow region, the axial and radial turbulence intensities are around 16% and 12% for the first two grids, but around 15% and 11% for the two others. As a result, the rms profiles obtained using gridz40B and gridz25B are closer to the measurements in Figure 12(c).

The effects of the grid on the spectral properties of velocity fluctuations are investigated by considering spectra at $r = r_0$. The spectra computed for the axial velocity fluctuations u_z' at $z = 10r_0$ for jetv0D0200 and jetv0D0025 and at $z = 15r_0$ for jetv9D0150 are presented in Figure 14 as a function of the Strouhal number St_D. Those from the previous LES studies using coarser grids are also plotted. In all cases, the spectra are dominated by low-frequency components at $St_D \simeq 0.1$. For jetv0D0200, in Figure 14(a), they do not appear to depend appreciably on the grid except in the high-frequency range due to the increase of the grid cut-off frequency as the mesh is refined. For the two other jets, the spectra also look similar

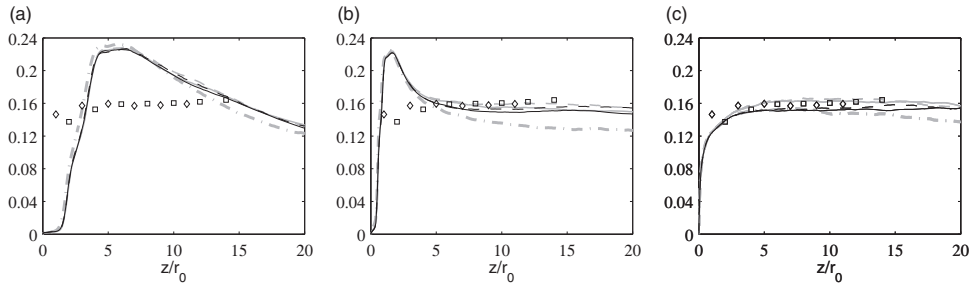

Figure 12. Variations of axial turbulence intensity $\langle u'_z u'_z \rangle^{1/2}/u_j$ obtained at $r = r_0$ for (a) jetv0D0200, (b) jetv0D0025 and (c) jetv9D0150 using ——— gridz60A, — — — gridz40A ——— gridz40B, — — — gridz25B, — · — · coarser grids (gridv0D0200old for jetv0D0200, gridv0D0025old for jetv0D0025 and gridv9D0150old for jetv9D0150) in previous studies; peak values measured in isothermal jets at M = 0.9 by ◇ Fleury[62] at $\mathrm{Re}_D = 7.7 \times 10^5$, and □ Castelain[63] at $\mathrm{Re}_D = 10^6$.

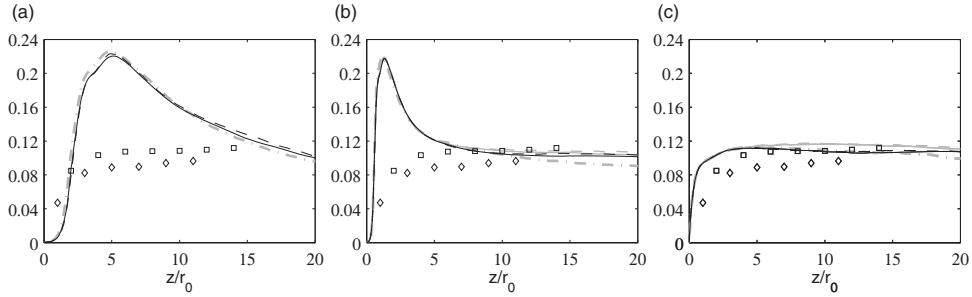

Figure 13. Variations of radial turbulence intensity $\langle u'_r u'_r \rangle^{1/2}/u_j$ obtained at $r = r_0$ for (a) jetv0D0200, (b) jetv0D0025 and (c) jetv9D0150; same line and symbol types as in Figure 12.

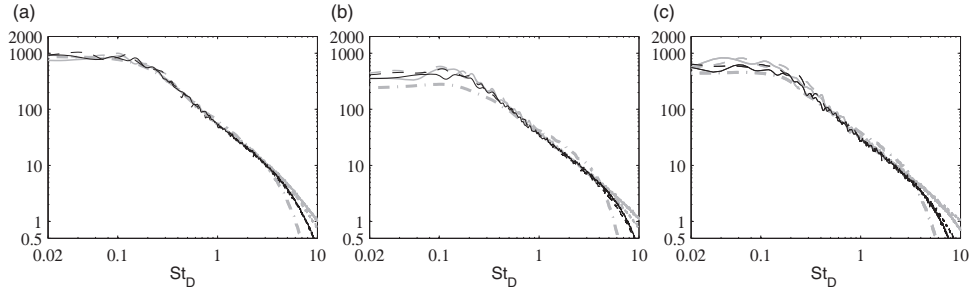

Figure 14. Power spectral densities of axial velocity fluctuations u'_z, multiplied with $10^4/u_j^2$, obtained at $r = r_0$ for (a) jetv0D0200 and (b) jetv0D0025 at $z = 10r_0$ and (c) jetv9D0150 at $z = 15r_0$, using ——— gridz60A, — — — gridz40A ——— gridz40B, — — — gridz25B, — · — · coarser grids (gridv0D0200old for jetv0D0200, gridv0D0025old for jetv0D0025 and gridv9D0150old for jetv9D0150) in previous studies, as a function of St_D.

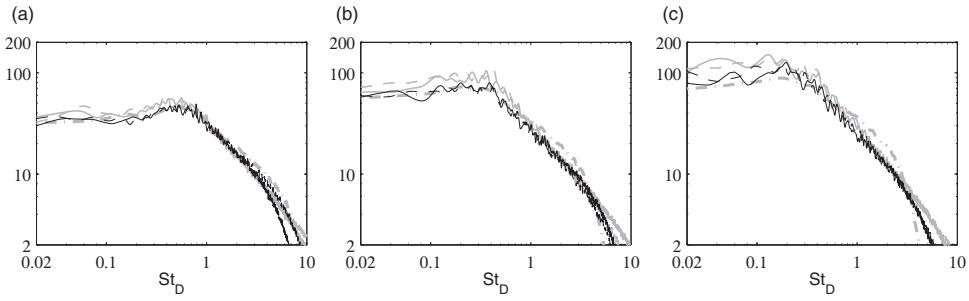

Figure 15. Power spectral densities of radial velocity fluctuations u_r', multiplied with $10^4/u_j^2$, obtained at $r = r_0$ for jetv9D0150 at (a) $z = 5r_0$, (b) $z = 10r_0$ and (c) $z = 15r_0$ using ——— gridz60A, — — — gridz40A ——— gridz40B, — — — gridz25B, — · — · gridv9D0150old, as a function of St_D.

at first sight, but show higher levels at low frequencies for the LES using finer grids in the mixing layers.

In order to shed more light on this counter-intuitive trend, the spectra evaluated for the radial velocity fluctuations u_r' at $z = 5r_0$, $10r_0$ and $15r_0$ for jetv9D0150 are shown in Figure 15. At the first position, in Figure 15(a), the low-frequency and peak components are slightly but noticeably stronger in the spectra of the LES using gridz40B and gridz25B. This is also the case at the two other positions in Figure 15(b,c). It appears however that the difference between the spectra at low frequencies increases with the axial distance as the turbulent structures are convected and evolved. Refining the grid in the early region of mixing-layer development therefore leads to stronger large-scale structures all along the jet flow. This result is consistent with the observation made on the vorticity fields of Figures 9 and 10, namely that coherent structures can be more easily seen in the turbulent mixing layers using gridz40B than using gridv9D0150old or gridz40A.

For completeness, the ratios $\delta_\theta/\Delta z$ and $L_{uu}^{(z)}/\Delta z$ of the shear-layer momentum thickness and the integral length scale at $r = r_0$ with the mesh spacing in the axial direction are depicted in Figure 16 for jetv9D0150, to assess the quality of discretization in the mixing layers of the initially disturbed jet. The integral length scale is here approximated by $2.1\delta_\theta$ according to the results obtained using gridv9D0150old.[30] The values of $\delta_\theta/\Delta z$ and $L_{uu}^{(u)}/\Delta z$ do not exceed 5 and 10 over $0 \leq z \leq 15r_0$ for gridv9D0150old, and over $0 \leq z \leq 5r_0$ for gridz60A and gridz40A. As expected, they are larger for gridz40B and gridz25B, and are equal, for instance, to 9 and 19 at $z = 5r_0$ for gridz40B. In view of what precedes, it seems therefore necessary, in order to properly compute turbulent high-Reynolds number jets, to use mesh spacings lower than $\delta_\theta/5$ and $L_{uu}^{(z)}/10$ all along the jet mixing layers.

Centerline flow properties

The variations of the centerline mean axial velocity in the three jets are presented in Figure 17. Experimental data for isothermal jets at $M = 0.9$ at $Re_D \geq 7.7 \times 10^5$ are also shown for the comparison. As noted in previous section, the jet flow development is more rapid in jetv0D0200 than in jetv0D0025 and jetv9D0150. This leads to a potential core ending at about $z_c = 9r_0$ in the first jet and $z_c = 15r_0$ in the two others, with z_c being defined as the axial distance at which the centerline mean velocity is equal to $0.95u_j$. For jetv0D0200,

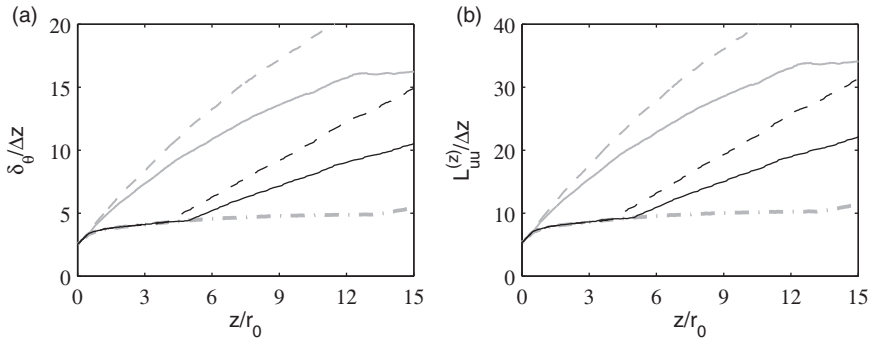

Figure 16. Variations of the ratios of (a) the shear-layer momentum thickness δ_θ and (b) the integral length scale $L_{uu}^{(z)}$ at $r = r_0$ with the mesh spacing in the axial direction Δz, obtained for jetv9D0150 using ——— gridz60A, — — — gridz40A ——— gridz40B, — — — gridz25B and — · — · gridv9D0150old. The integral length scale is approximated[30] by $2.1\delta_\theta$.

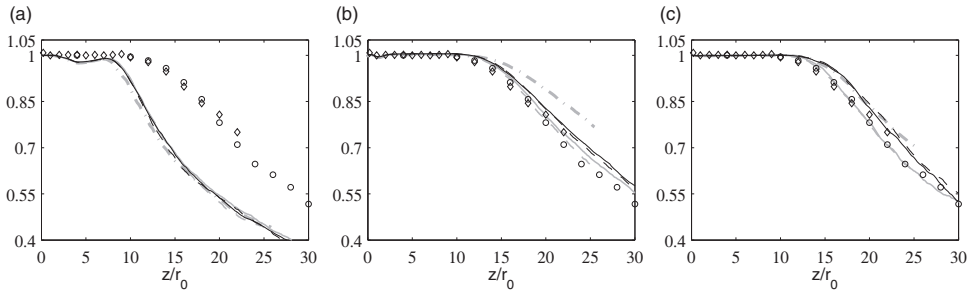

Figure 17. Variations of mean axial velocity $\langle u_z \rangle / u_j$ obtained at $r = 0$ for (a) jetv0D0200, (b) jetv0D0025 and (c) jetv9D0150 using ——— gridz60A, — — — gridz40A ——— gridz40B, — — — gridz25B, — · — · coarser grids (gridv0D0200old for jetv0D0200, gridv0D0025old for jetv0D0025 and gridv9D0150old for jetv9D0150) in previous studies; measurements for isothermal jets at M = 0.9 of ○ Lau et al.[64] at $Re_D = 10^6$, and ◇ Fleury et al.[65] at $Re_D = 7.7 \times 10^5$.

in Figure 17(a), the velocity profiles from the present and previous LES are very similar to each others. For the two other jets, on the contrary, significant differences appear. Overall, as the grid is refined, the jet potential core is shorter. This is clearly visible for jetv0D0025 in Figure 17(b), where $z_c = 16.8r_0$ using gridv0D0025old but $z_c \simeq 15r_0$ using the four new grids. The velocity decay downstream of the potential core is also slower using gridv0D0025old, which may be related to the poor mixing of the shear-layer turbulent structures that seems to happen on the jet axis in Figure 7(a). In addition, the velocity decay starts earlier using gridz40B and gridz25B than using gridz60A and gridz40A. This is particularly true for the initially disturbed jet in Figure 17(c), which is consistent with the variations of the shear-layer momentum thickness of Figure 11(c). As a consequence, the end of the potential core for jetv9D0150 moves from $z_c \simeq 16r_0$ down to $z_c \simeq 15r_0$, and the velocity profiles are closer to the measurements.

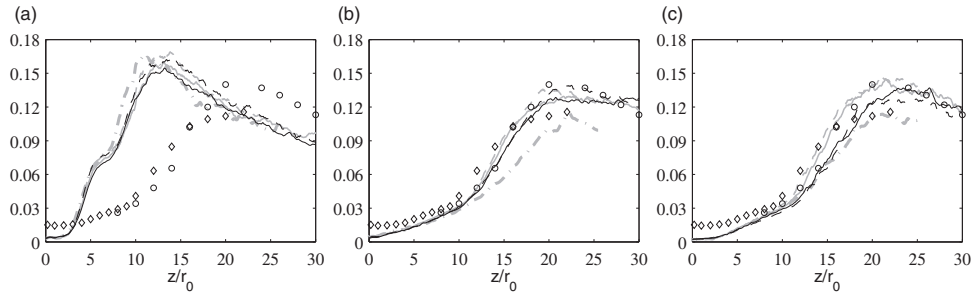

Figure 18. Variations of axial turbulence intensity $\langle u_z' u_z' \rangle^{1/2}/u_j$ obtained at $r = 0$ for (a) jetv0D0200, (b) jetv0D0025 and (c) jetv9D0150; same line and symbol types as in Figure 17.

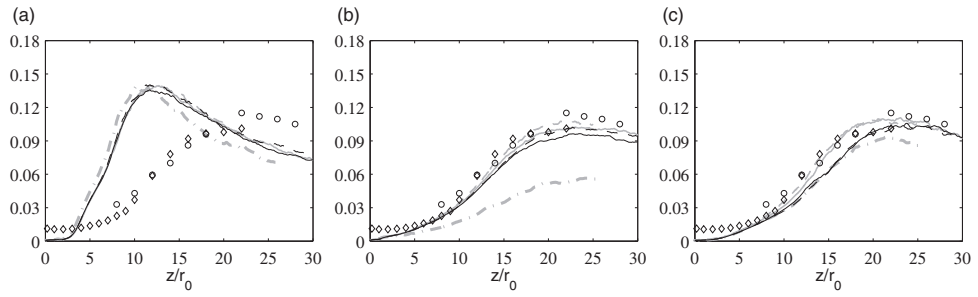

Figure 19. Variations of radial turbulence intensity $\langle u_r' u_r' \rangle^{1/2}/u_j$ obtained at $r = 0$ for (a) jetv0D0200, (b) jetv0D0025 and (c) jetv9D0150; same line and symbol types as in Figure 17.

The variations of the axial and radial turbulence intensities along the jet centerline between $z = 0$ and $z = 30r_0$ are plotted in Figures 18 and 19, together with measurements for isothermal, high Reynolds number jets at M = 0.9. Despite the fact that they may not be well converged because of the impossibility of averaging in the azimuthal direction, especially for jetv9D0150 simulated over a time period of $300r_0/u_j$, clear trends emerge. They are similar to those found previously for the turbulence intensities along the nozzle-lip line in Figures 12 and 13. Indeed, for jetv0D0200, the results do not strongly vary with the grid, whereas for the two other jets, the turbulence intensities increase as the grid is finer in the jet mixing layers. For jetv0D0025, their maximum values are only of 11.4% for u_z' and 5.6% for u_r' using gridv0D0025old, but of about 13.8% and 10.6% using gridz40B and gridz25B. The very low levels of radial velocity fluctuations in the first case are most likely due to the lack of turbulent structures on the centerline revealed in Figure 7(a). One reason for that may be the effective number of points of only $n_\theta^{axis} = 8$ in the azimuthal direction close to the jet axis, reported in Table 2. In addition, the rms velocity peaks are reached earlier, and are higher using gridz40B and gridz25B than using gridz60A and gridz40A. For jetv9D0150, for instance, the peak values are around 13.5% for u_z' and 10.5% for u_r' with the latter two grids, but 14.7% and 11.2% with the two others, which is better in line with the measurements. Therefore, refining the mesh grid downstream of the nozzle exit turns out to be beneficial for the computation of both the mixing layer and the flow developments.

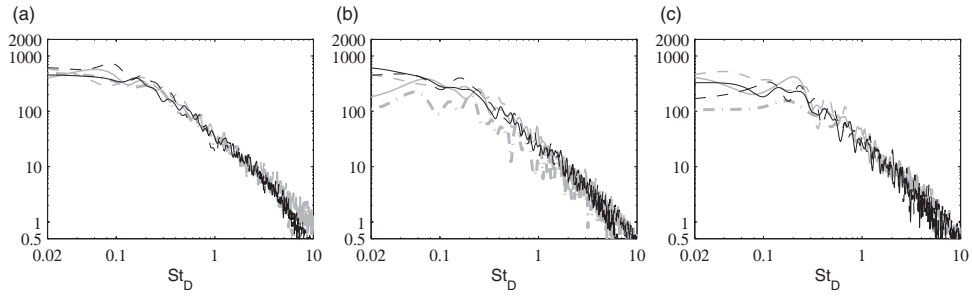

Figure 20. Power spectral densities of axial velocity fluctuations u_z', multiplied with $10^4/u_j^2$, obtained at $r = 0$ for (a) jetv0D0200 at $z = 15r_0$, and for (b) jetv0D0025 and (c) jetv9D0150 at $z = 20r_0$, using ——— gridz60A, — — — gridz40A ——— gridz40B, — — — gridz25B, — · — · coarser grids (gridv0D0200old for jetv0D0200, gridv0D0025old for jetv0D0025 and gridv9D0150old for jetv9D0150) in previous studies; as a function of St_D.

Finally, the spectra of axial velocity fluctuations calculated on the jet axis at $z = 15r_0$ for jetv0D0200 and at $z = 20r_0$ for jetv0D0025 and jetv9D0150, that is near the turbulence intensity peaks, are presented in Figure 20 as a function of St_D. As pointed out above, they may not be very well converged, especially for jetv9D0150 for which the simulation time includes only 15 periods associated with $St_D = 0.1$, which may cause some of the discrepancies observed for $St_D < 0.1$. Despite this, the spectra obtained for jetv0D0200 are very much alike, and those for jetv0D0025 and jetv9D0150 seem to contain more energetic low-frequency components using finer grids. As is the case along the nozzle-lip line, see the results of the previous section, stronger large-scale structures are thus present on the centerline of these two jets in the present LES, as more fine-scale turbulence, necessary for obtaining the correct dynamics of these structures, is computed.

Jet acoustic fields

Pressure snapshots

Snapshots of the vorticity norm and of the fluctuating pressure obtained for the three jets in the LES using gridz60A with physical extents of $L_r = 20r_0$ and $L_z = 60r_0$ in the radial and axial directions are represented in Figure 21 for $r \leq 4r_0$ and $r \geq 4r_0$, respectively. In agreement with previous studies,[27,30] the acoustic levels are greater for the two initially fully laminar jets than for the initially disturbed jet. They are typically of the order of 90 Pa for jetv0D0200, 60 Pa for jetv0D0025 and 40 Pa for jetv9D0150. This is due to the fact that circular acoustic waves of high amplitude are generated by vortex pairings early on in the mixing layers of the first two jets. The associated wavelengths of these waves are shorter in jetv0D0025 than in jetv0D0200 because of the thinner nozzle-exit boundary layers in the former case. Farther downstream, large-scale near-field pressure fluctuations, classically attributed to the flow coherent structures,[57] are observed in the close vicinity of the jets. In addition, strong low-frequency waves propagating in the downstream direction are also found in all cases, see in Figure 21(c) for the jet which does not radiate vortex-pairing noise.

The far field calculated for jetv9D0150 with highly disturbed initial flow conditions is illustrated in Figure 3 providing a snapshot of the vorticity issued from the LES

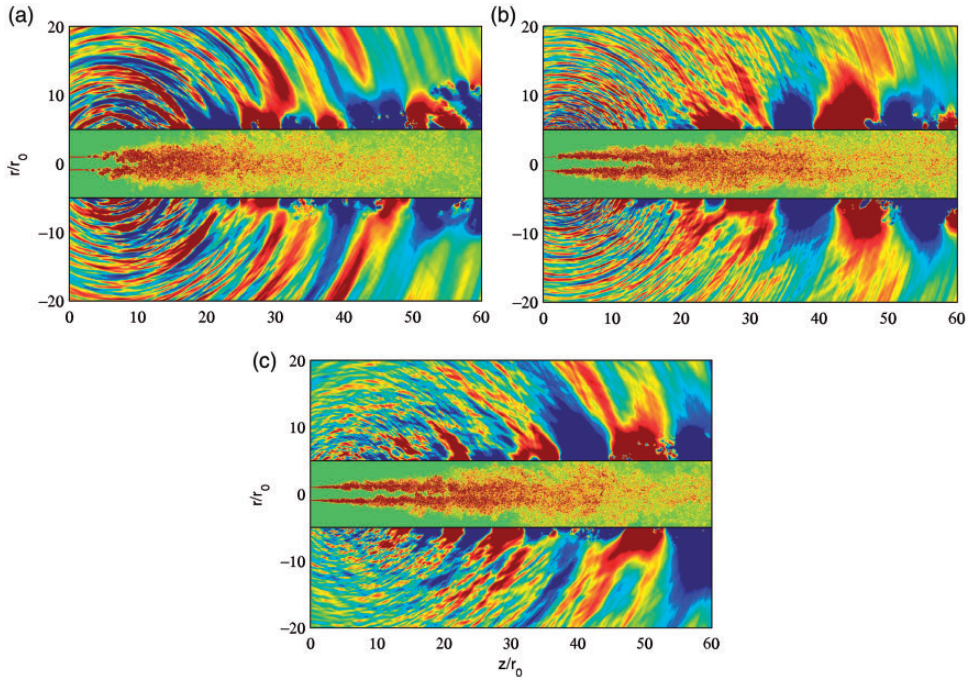

Figure 21. Representation of vorticity norm inside the jet flow and of pressure fluctuations outside, obtained for (a) jetv0D0200, (b) jetv0D0025 and (c) jetv9D0150 using gridz60A. The color scales range up to the level of $4u_j/r_0$ for vorticity, and (a) from −90 to 90 Pa, (b) from –60 to 60 Pa, and (c) from –40 to 40 Pa for pressure (See colour version of this figure online).

using gridz60A and of the pressure computed by solving the ILEEs from the LES data at $z = -1.5r_0$, $r = L_r = 20r_0$ and $z = L_z = 60r_0$. The two main features of subsonic jet noise[13,37–39] appear clearly. The first one is the pronounced directivity in the downstream direction with a peak angle around $\varphi = 30$ degrees relative to the jet axis. The second one is the change in spectral content with the radiation angle. In particular, very low-frequency components characterized by wavelengths $\lambda \simeq 15r_0$, yielding Strouhal numbers $\mathrm{St}_D \simeq 0.15$, are dominant for shallow angles, which does not seem to be the case for wide angles.

In order to give a first glimpse of the influence of the mesh on the pressure field, the LES results obtained for jetv9D0150 using gridz60A and gridz40B up to $r = L_r = 15r_0$ and $z = L_z = 40r_0$ are shown in Figure 22. Their properties look very similar. The pressure levels may however be slightly higher for the LES performed with gridz40B in Figure 22(b), notably in the sideline direction.

Far-field acoustic spectra

The pressure spectra evaluated at a distance of $150r_0$ of the nozzle exit for the angles $\varphi = 40$, 60, 90 and 120 degrees relative to the jet direction, by solving the ILEE from the LES near-field data, are represented in Figures 23 to 26, respectively. They are compared with the results of previous simulations using coarser grids, and with the experimental data acquired by Bridges and Brown[16] at the same distance for an isothermal jet at $\mathrm{M} = 0.9$ and

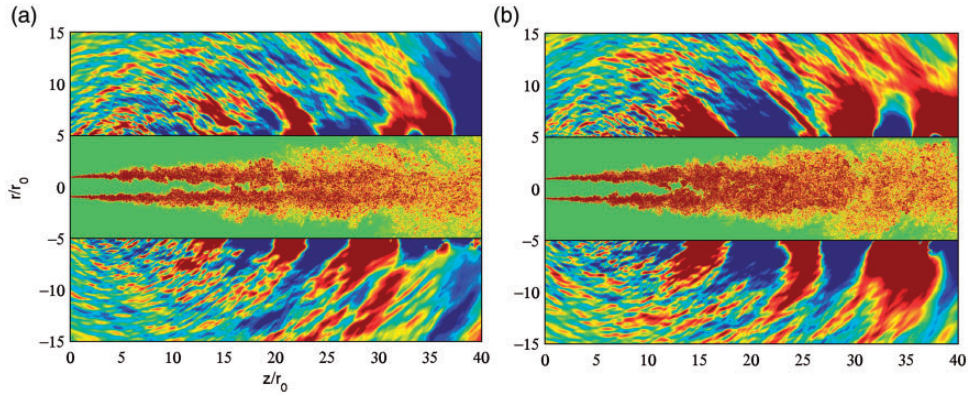

Figure 22. Representation of vorticity norm inside the jet flow and of pressure fluctuations outside, obtained for jetv9D0150 using (a) gridz60A and (b) gridz40B. The color scales range up to the level of $4u_j/r_0$ for vorticity, and from –40 to 40 Pa for pressure (See colour version of this figure online).

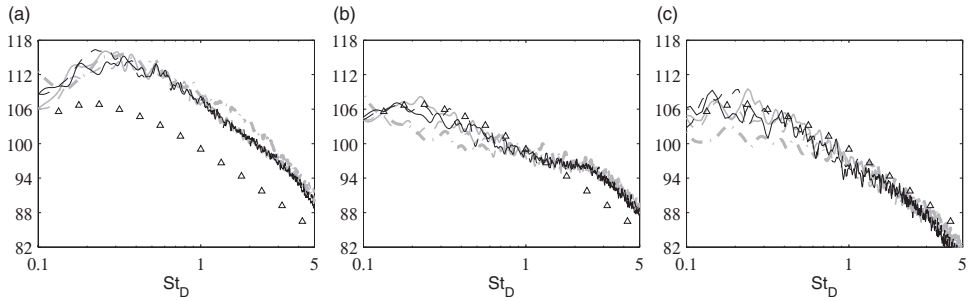

Figure 23. Sound pressure levels obtained at $150r_0$ from the nozzle exit and $\varphi = 40$ degrees relative to the jet direction for (a) jetv0D0200, (b) jetv0D0025 and (c) jetv9D0150 using ——— gridz60A, – – – gridz40A ——— gridz40B, – – – gridz25B, – · – · coarser grids (gridv0D0200old for jetv0D0200, gridv0D0025old for jetv0D0025 and gridv9D0150old for jetv9D0150) in previous studies, as a function of St_D, in dB/St_D; △ measurements of Bridges and Brown[16] for an isothermal jet at $M = 0.9$ and $Re_D = 10^6$.

$Re_D = 10^6$. As expected, the shape of the spectra varies significantly with the radiation angle. They are less dominated by low-frequency components at wider angles. Additional noise components are also noted in the spectra of the two initially laminar jets compared to the initially highly disturbed jet. They are well visible in the spectra at $\varphi = 90$ degrees of Figure 25(a,b), for instance. They are centered around a Strouhal number of $St_D = 0.5$ for jetv00D0200 and of $St_D = 2$ for jetv0D0025, which correspond to the frequencies of the first stage of vortex pairings in the initially laminar mixing layers of the jets.

Comparing the spectra obtained with the various grids, they do not differ much from each other for jetv0D0200, but they display significant discrepancies for the two other jets at all radiation angles. This is not surprising given the grid sensitivity of the velocity flow fields documented in the preceding sections. For jetv0D0025 and jetv9D0150, more precisely, the spectra are nearly superimposed for $St_D \geq 0.5$. However, they contain stronger components for $St_D \leq 0.5$ as the grid is refined, with the exception of the spectrum at $\varphi = 40$ degrees for

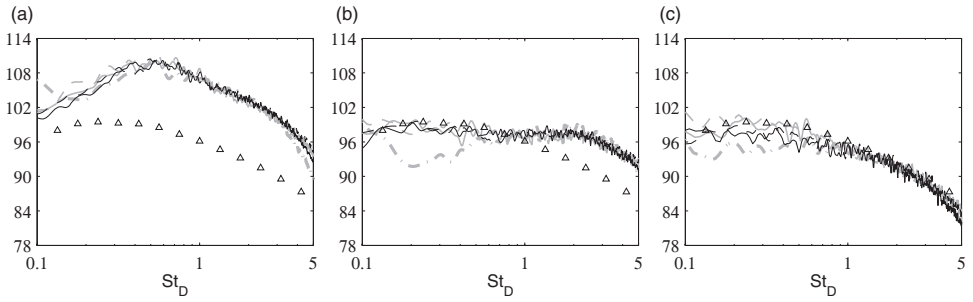

Figure 24. Sound pressure levels obtained at $150r_0$ from the nozzle exit and $\varphi = 60$ degrees relative to the jet direction for (a) jetv0D0200, (b) jetv0D0025 and (c) jetv9D0150, as a function of St_D, in dB/St_D; same line and symbol types as in Figure 23.

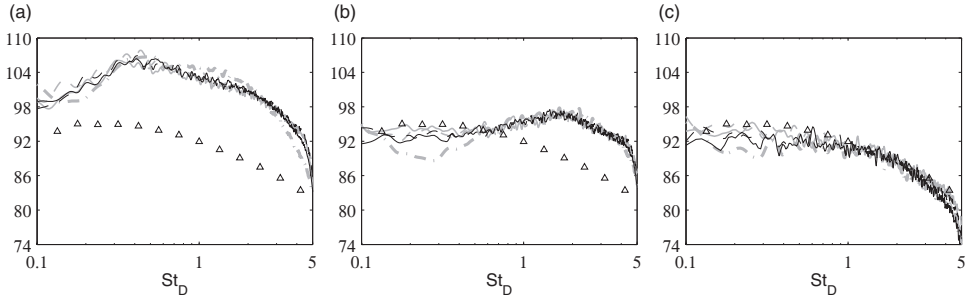

Figure 25. Sound pressure levels obtained at $150r_0$ from the nozzle exit and $\varphi = 90$ degrees relative to the jet direction for (a) jetv0D0200, (b) jetv0D0025 and (c) jetv9D0150, as a function of St_D, in dB/St_D; same line and symbol types as in Figure 23.

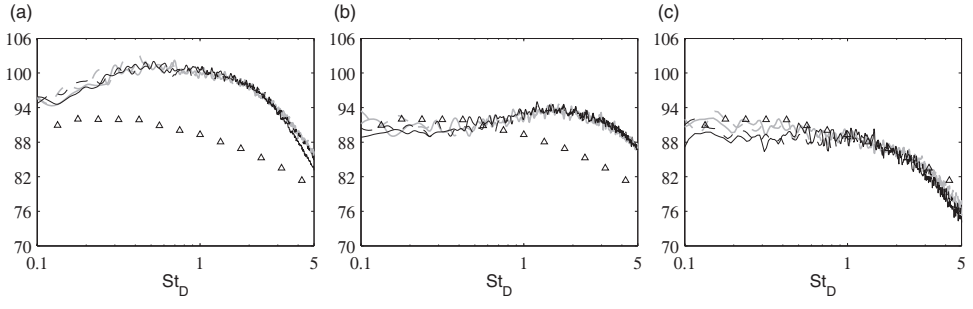

Figure 26. Sound pressure levels obtained at $150r_0$ from the nozzle exit and $\varphi = 120$ degrees relative to the jet direction for (a) jetv0D0200, (b) jetv0D0025 and (c) jetv9D0150, as a function of St_D, in dB/St_D; same line and symbol types as in Figure 23.

the LES using gridz25B most likely due to the fact that the surface employed for the far-field extrapolation is open in the downstream direction. Excluding this, for such Strouhal numbers, a difference of 3–4 dB is observed between the present LES and the previous simulations using much coarser grids, A gain by about 1–2 dB is even noted between the LES using gridz40B and gridz25B and those using gridz60A and gridz40A. The increase in grid resolution all along the jet mixing layers, which results in higher turbulence intensities and stronger large-scale structures in the jet flow, thus leads to more low-frequency noise, and to a better match with the measurements at low Strouhal numbers. As a consequence, a good agreement with the experimental data is found for $St_D \leq 0.8$ for the initially laminar jet with thin nozzle-exit boundary layers, see in Figures 23(b) and 25(b) at $\varphi = 40$ and 90 degrees, and over the whole frequency range for the initially highly disturbed jet, see in Figures 24(c) and 26(c) at $\varphi = 60$ and 120 degrees, for instance.

Conclusion

Three isothermal round jets at a Mach number of 0.9 and a Reynolds number of 10^5 with controlled nozzle-exit conditions, namely two initially fully laminar jets and an initially highly disturbed jet, are computed by LES using four cylindrical grids in order to investigate the influence of the grid point distribution on the jet flow, near and far acoustic fields.

Compared to the results from previous studies using coarser grids, the present results are found to be comparable for the initially laminar jet with thick nozzle-exit boundary layers, but significantly different for the initially laminar jet with thin boundary layers and for the initially disturbed jet. In the latter two cases, the use of a finer grid resolution in the jet flow leads to a more rapid jet development and to higher turbulence intensities in the mixing layers and in the vicinity of the end of the potential core. More surprisingly, this also results in the presence of stronger large-scale structures, and in the generation of more low-frequency noise. Despite the difference in Reynolds number, a good agreement with experimental data available for laboratory-scale jets at Reynolds numbers of the order of 10^6 is thus obtained for grids (gridz40B and gridz25B) with very small mesh spacings in the region of early development of the jet mixing layers. The simulations performed using these grids consequently provide solutions which could be used in the future in order to validate simulations, but also to investigate noise generation mechanisms in subsonic jets. For that purpose, the computations made using gridz40B, of larger size in the axial direction than gridz25B, will be extended in time in order to collect flow and acoustic signals over longer periods, typically of $1000 r_0/u_j$.

Finally, the present study highlights the importance of the largest turbulent scales, also referred to as coherent structures, in free shear flows. Given their essential role in terms of flow development and sound production, these structures must be accurately taken into account in numerical simulations. For that, the mesh grids must be fine enough that they are well discretized, which is generally relatively easy to guarantee when the properties of the numerical schemes are known. The grids must also allow them to form and evolve properly, which is more difficult to ensure a priori given the lack of well-established rules about that point. However, this study clearly suggests that in some cases, including the last two subsonic jets simulated, the computation of a wide range of fine-scale structures is required to correctly capture the generation and dynamics of the flow coherent structures. This is the main original result of this work.

Acknowledgements

This work was granted access to the HPC resources of FLMSN (Fédération Lyonnaise de Modélisation et Sciences Numériques), partner of EQUIPEX EQUIP@MESO, and of the resources of CINES (Centre Informatique National de l'Enseignement Supérieur) and IDRIS (Institut du Développement et des Ressources en Informatique Scientifique) under the allocation 2016-2a0204 made by GENCI (Grand Equipement National de Calcul Intensif). The author gratefully acknowledges Dr Olivier Marsden for his crucial help in developing the numerical code used in this study.

Declaration of conflicting interests

The author(s) declared no potential conflicts of interest with respect to the research, authorship, and/or publication of this article.

Funding

The author(s) disclosed receipt of the following financial support for the research, authorship, and/or publication of this article: This work was performed within the framework of the Labex CeLyA of Université de Lyon, operated by the French National Research Agency (Grant No. ANR-10-LABX-0060/ANR-11-IDEX-0007).

References

1. Tam CKW. Computational aeroacoustics: Issues and methods. *AIAA J* 1995; 33: 1788–1796.
2. Colonius T and Lele SK. Computational aeroacoustics: Progress on nonlinear problems of sound generation. *Prog Aerosp Sci* 2004; 40: 345–416.
3. Bailly C and Bogey C. Contributions of CAA to jet noise research and prediction. *Int J Comput Fluid Dyn* 2004; 18: 481–491.
4. Wang M, Freund JB and Lele SK. Computational prediction of flow-generated sound. *Annu Rev Fluid Mech* 2006; 38: 483–512.
5. Bodony DJ and Lele SK. On the current status of jet noise predictions using large-eddy simulation. *AIAA J* 2008; 46: 364–380.
6. Shur ML, Spalart PR and Strelets MK. LES-based evaluation of a microjet noise reduction concept in static and flight conditions. *J Sound Vib* 2011; 330: 4083–4097.
7. Fosso Pouangué A, Sanjosé M, Moreau S, et al. Subsonic jet noise simulations using both structured and unstructured grids. *AIAA J* 2015; 53: 55–69.
8. Bogey C and Marsden O. Simulations of initially highly disturbed jets with experiment-like exit boundary layers. *AIAA J* 2016; 54: 1299–1312.
9. Brès GA, Jaunet VL, Rallic M, et al. Large eddy simulation for jet noise: The importance of getting the boundary layer right. In: *AIAA paper 2015-2535*, 2015.
10. Bogey C, Bailly C and Juvé D. Noise investigation of a high subsonic, moderate Reynolds number jet using a compressible LES. *Theor Comput Fluid Dyn* 2003; 16: 273–297.
11. Panda J, Seasholtz RG and Elam KA. Investigation of noise sources in high-speed jets via correlation measurements. *J Fluid Mech* 2005; 537: 349–385.
12. Bogey C and Bailly C. An analysis of the correlations between the turbulent flow and the sound pressure field of subsonic jets. *J Fluid Mech* 2007; 583: 71–97.
13. Tam CKW, Viswanathan K, Ahuja KK, et al. The sources of jet noise: Experimental evidence. *J Fluid Mech* 2008; 615: 253–292.
14. Bridges J and Wernet MP. Validating large-eddy simulation for jet aeroacoustics. *J Propul Power* 2012; 28: 226–234.
15. Viswanathan K. Jet aeroacoustic testing: Issues and implications. *AIAA J* 2003; 41: 1674–1689.

16. Bridges J and Brown CA. Validation of the small hot jet acoustic rig for aeroacoustics. In: *AIAA paper 2005-2846*, 2005.
17. Brown C and Bridges J. Small hot jet acoustic rig validation. In: *Nasa Tm-2006-214234*, 2006.
18. Bridges J and Wernet MP. Establishing consensus turbulence statistics for hot subsonic jets. In: *AIAA paper 2010-3751*, 2010.
19. Viswanathan K. Aeroacoustics of hot jets. *J Fluid Mech* 2004; 516: 39–82.
20. Harper-Bourne M. Jet noise measurements: Past and present. *Int J Aeroacoust* 2010; 9: 559–588.
21. Freund JB. Noise sources in a low-Reynolds-number turbulent jet at Mach 0.9. *J Fluid Mech* 2001; 438: 277–305.
22. Sandberg RD, Sandham ND and Suponitsky V. DNS of compressible pipe flow exiting into a coflow. *Int J Heat Fluid Flow* 2012; 35: 33–44.
23. Bühler S, Kleiser L and Bogey C. Simulation of subsonic turbulent nozzle-jet flow and its near-field sound. *AIAA J* 2014; 52: 1653–1669.
24. Zaman KBMQ. Effect of initial condition on subsonic jet noise. *AIAA J* 1985; 23: 1370–1373.
25. Zaman KBMQ. Far-field noise of a subsonic jet under controlled excitation. *J Fluid Mech* 1985; 152: 83–111.
26. Bridges JE and Hussain AKMF. Roles of initial conditions and vortex pairing in jet noise. *J Sound Vib* 1987; 117: 289–311.
27. Bogey C and Bailly C. Influence of nozzle-exit boundary-layer conditions on the flow and acoustic fields of initially laminar jets. *J Fluid Mech* 2010; 663: 507–539.
28. Bogey C, Marsden O and Bailly C. Influence of initial turbulence level on the flow and sound fields of a subsonic jet at a diameter-based Reynolds number of 10^5. *J Fluid Mech* 2012; 701: 352–385.
29. Shur ML, Spalart PR and Strelets MK. Noise prediction for increasingly complex jets. Part I: Methods and tests. *Int J Aeroacoust* 2005; 4: 213–246.
30. Bogey C, Marsden O and Bailly C. Large-eddy simulation of the flow and acoustic fields of a Reynolds number 10^5 subsonic jet with tripped exit boundary layers. *Phys Fluids* 2011; 23: 035104.
31. Grosche FR. Distributions of sound source intensities in subsonic and supersonic jets. In: *AGARD-CP-131*, 1974, pp.4–1 to 4–10.
32. Chu WT and Kaplan RE. Use of a spherical concave reflector for jet-noise-source distribution diagnosis. *J Acoust Soc Am* 1976; 59: 1268–1277.
33. Fisher MJ, Harper-Bourne M and Glegg SAL. Jet engine noise source location: The polar correlation technique. *J Sound Vib* 1977; 51: 23–54.
34. Ahuja KK, Massey KC and D'agostino MS. A simple technique of locating noise sources of a jet under simulated forward motion. In: *AIAA paper 98-2359*, 1998.
35. Narayanan S, Barber TJ and Polak DR. High subsonic jet experiments: Turbulence and noise generation studies. *AIAA J* 2002; 40: 430–437.
36. Lee SS and Bridges J. Phased-array measurements of single flow hot jets. In: *Nasa/Tm 2005-213826*, 2005.
37. Bogey C, Barré S, Fleury V, et al. Experimental study of the spectral properties of near-field and far-field jet noise. *Int J Aeroacoust* 2007; 6: 73–92.
38. Mollo-Christensen E, Kolpin MA and Martucelli JR. Experiments on jet flows and jet noise far-field spectra and directivity patterns. *J Fluid Mech* 1964; 18: 285–301.
39. Zaman KBMQ and Yu JC. Power spectral density of subsonic jet noise. *J Sound Vib* 1985; 98: 519–537.
40. Crow SC and Champagne FH. Orderly structure in jet turbulence. *J Fluid Mech* 1971; 48: 547–591.
41. Bogey C, Marsden O and Bailly C. On the spectra of nozzle-exit velocity disturbances in initially nominally turbulent jets. *Phys Fluids* 2011; 23: 091702.
42. Bogey C, Marsden O and Bailly C. Effects of moderate Reynolds numbers on subsonic round jets with highly disturbed nozzle-exit boundary layers. *Phys Fluids* 2012; 24: 105107.

43. Bogey C and Marsden O. Identification of the effects of the nozzle-exit boundary-layer thickness and its corresponding Reynolds number in initially highly disturbed subsonic jets. *Phys Fluids* 2013; 25: 055106.
44. Mohseni K and Colonius T. Numerical treatment of polar coordinate singularities. *J Comput Phys* 2000; 157: 787–795.
45. Bogey C, de Cacqueray N and Bailly C. Finite differences for coarse azimuthal discretization and for reduction of effective resolution near origin of cylindrical flow equations. *J Comput Phys* 2011; 230: 1134–1146.
46. Bogey C and Bailly C. A family of low dispersive and low dissipative explicit schemes for flow and noise computations. *J Comput Phys* 2004; 194: 194–214.
47. Bogey C, de Cacqueray N and Bailly C. A shock-capturing methodology based on adaptative spatial filtering for high-order non-linear computations. *J Comput Phys* 2009; 228: 1447–1465.
48. Berland J, Bogey C, Marsden O, et al. High-order, low dispersive and low dissipative explicit schemes for multi-scale and boundary problems. *J Comput Phys* 2007; 224: 637–662.
49. Tam CKW and Dong Z. Radiation and outflow boundary conditions for direct computation of acoustic and flow disturbances in a nonuniform mean flow. *J Comp Acous* 1996; 4: 175–201.
50. Bogey C and Bailly C. Three-dimensional non reflective boundary conditions for acoustic simulations: Far-field formulation and validation test cases. *Acta Acust United Acust* 2002; 88: 463–471.
51. Bogey C and Bailly C. Large eddy simulations of transitional round jets: Influence of the Reynolds number on flow development and energy dissipation. *Phys Fluids* 2006; 18: 065101.
52. Bogey C and Bailly C. Turbulence and energy budget in a self-preserving round jet: Direct evaluation using large-eddy simulation. *J Fluid Mech* 2009; 627: 129–160.
53. Fauconnier D, Bogey C and Dick E. On the performance of relaxation filtering for large-eddy simulation. *J Turbulence* 2013; 14: 22–49.
54. Kremer F and Bogey C. Large-eddy simulation of turbulent channel flow using relaxation filtering: Resolution requirement and Reynolds number effects. *Comput Fluids* 2015; 116: 17–28.
55. Bogey C, Barré S, Juvé D, et al. Simulation of a hot coaxial jet: Direct noise prediction and flow-acoustics correlations. *Phys Fluids* 2009; 21: 035105.
56. de Cacqueray N and Bogey C. Noise of an overexpanded Mach 3.3 jet: Non-linear propagation effects and correlations with flow. *Int J Aeroacoust* 2014; 13: 607–632.
57. Arndt REA, Long DF and Glauser MN. The proper orthogonal decomposition of pressure fluctuations surrounding a turbulent jet. *J Fluid Mech* 1997; 340: 1–33.
58. Ahuja KK, Tester BJ and Tanna HK. Calculation of far field jet noise spectra from near field measurements with true source location. *J Sound Vib* 1987; 116: 415–426.
59. Viswanathan K. Distributions of noise sources in heated and cold jets: Are they different? *Int J Aeroacoust* 2006; 9: 589–626.
60. Zaman KBMQ. Effect of initial boundary-layer state on subsonic jet noise. *AIAA J* 2012; 50: 1784–1795.
61. Brown GL and Roshko A. On density effects and large structure in turbulent mixing layers. *J Fluid Mech* 1974; 64: 775–816.
62. Fleury V. *Superdirectivité, bruit d'appariement et autres contributions au bruit de jet subsonique*. PhD Thesis No. 2006-18, Ecole Centrale De Lyon, France, 2006.
63. Castelain T. Contrôle de jet par microjets impactants. mesure de bruit rayonné et analyse aérodynamique. PhD Thesis No. 2006-33, Ecole Centrale de Lyon, France, 2006.
64. Lau JC, Morris PJ and Fisher MJ. Measurements in subsonic and supersonic free jets using a laser velocimeter. *J Fluid Mech* 1979; 93: 1–27.
65. Fleury V, Bailly C, Jondeau E, et al. Space–time correlations in two subsonic jets using dual-PIV measurements. *AIAA J* 2008; 46: 2498–2509.